Crystallization Characteristics and In-Mold Performance of Electroslag Remelting-Type TiO_2-Bearing Slag

DINGLI ZHENG, JING LI, CHENGBIN SHI, and JIANTAO JU

The non-isothermal crystallization characteristics of the electroslag remelting (ESR)-type TiO_2-bearing slag were studied. The effect of crystallization characteristics of the slag on the in-mold performance was verified by ESR pilot trials operating in a static mode. The results showed that increasing TiO_2 content decreased the crystallization temperature and liquidus temperature of the slag and suppressed the crystallization tendency of the slag. There is no change in the types of the crystalline phases in the slag with different TiO_2 contents during cooling, *i.e.*, $11CaO{\cdot}7Al_2O_3{\cdot}CaF_2$, $CaTiO_3$, and CaF_2. The sequence of crystal precipitation during cooling was $11CaO{\cdot}7Al_2O_3{\cdot}CaF_2$ to $CaTiO_3$, and then CaF_2 with increasing TiO_2 content from 4.2 to 12.6 mass pct. With adding 16.8 mass pct TiO_2 in the slag, the precipitation of $11CaO{\cdot}7Al_2O_3{\cdot}CaF_2$ and $CaTiO_3$ took place simultaneously, followed by CaF_2. With the increase in the TiO_2 content from 4.2 to 16.8 mass pct in the slag, the dominant crystalline phase changed from $11CaO{\cdot}7Al_2O_3{\cdot}CaF_2$ to $CaTiO_3$. The morphology of $11CaO{\cdot}7Al_2O_3{\cdot}CaF_2$ and $CaTiO_3$ changed from faceted and bonelike to elliptically faceted and blocky, respectively. The morphology of CaF_2 were spherical in all cases, irrespective of TiO_2 contents in the slag. The decrease in the crystallization tendency of the slag with increasing TiO_2 contents was attributed to the decrease in the activity of CaO in the slag. The increasing of TiO_2 content in the slag are favorable for providing thin slag skin and stable heat flux across the slag skin, which improved the surface quality of the as-cast ESR ingot as demonstrated by ESR pilot trials operating in a static mode.

https://doi.org/10.1007/s11663-019-01536-w

I. INTRODUCTION

ELECTROSLAG remelting (ESR) is a secondary refining technique used for the production of some varieties of high-grade specialty steels and alloys. Slag plays an important role in the ESR process. For example, (1) the slag refines the liquid metal such as by removal of harmful elements and nonmetallic inclusions,[1,2] (2) the slag reacts with liquid metal to adjust the compositions of the ingot,[3,4] and (3) the slag film plays a key role in controlling horizontal heat transfer in the mold and providing lubrication for drawing-ingot-type ESR,[5] which could provide a sound condition for the good surface quality of as-cast ingot.[6]

In the production of Ti-containing steel and alloy by ESR, the TiO_2 content in the slag gradually increases during ESR process because of the introduction of the oxidation products of titanium from liquid metal into the slag pool. ESR industrial production practices showed that the TiO_2 content in the slag increased by about 20 pct in many cases.[7–9] The continuous increasing of TiO_2 content in the slag pool causes the change in the thermophysical properties of slag, such as crystallization behavior of the slag, which lead to ever-changing horizontal heat transfer in molds through slag films.[10,11] This frequently causes unstable operation and poor surface quality of the as-cast ingot during ESR production.[12] To stabilize the surface quality of as-cast ingot, it is necessary to carry out the research on the crystallization behavior of ESR-type slag with varying TiO_2 contents.

Many efforts have been carried out to study the crystallization behavior of TiO_2-bearing metallurgical slag. Shi *et al.*[13] studied the effect of TiO_2 addition on the isothermal crystallization behavior of the conventional high fluoride CaF_2-CaO-Al_2O_3 slag system and found that the addition of 8.1 mass pct TiO_2 largely enhanced the slag crystallization and suppressed the

DINGLI ZHENG, JING LI, and CHENGBIN SHI are with the State Key Laboratory of Advanced Metallurgy, University of Science and Technology Beijing (USTB), Beijing 100083, P.R. China. Contact email: lijing@ustb.edu.cn, chengbin.shi@ustb.edu.cn JIANTAO JU is with the School of Metallurgical Engineering, Xi'an University of Architecture and Technology, Xi'an 710055, P.R. China.

Manuscript submitted July 23, 2018.
Article published online March 11, 2019.

fluoride evaporation from the slag melt. Li *et al.*[14] found that the overall crystallization of mold fluxes was promoted with the addition of TiO_2 content. Silva *et al.*[15] showed that TiO_2 is likely to reduce the effect of MgO on the crystallization of $CaO\text{-}SiO_2\text{-}Al_2O_3$-based mold fluxes because of the strong glass former characteristic of TiO_2. Hao *et al.*[16] demonstrated that increasing the TiO_2 content from 0 to 12 mass pct resulted in a decrease of the melting temperature and solidification temperature of mold fluxes in titanium-stabilized stainless steel. Bothma and Pistorius[17] reported that lower TiO_2 content (< 6 pct) decreased the overall liquidus temperature of mold fluxes, which increased rapidly again at higher levels of TiO_2 pickup. Hu *et al.*[18] found that the initial crystallization temperature of the slag increased and then decreased with the increase in TiO_2 content in the slag with the basicity of 1. However, the effect of different TiO_2 contents in the slag during the ESR process on the non-isothermal crystallization behavior of ESR-type slag has not been reported yet.

This work attempts to ascertain the influence of TiO_2 content in the slag on the surface quality of as-cast ingot. Differential scanning calorimetry (DSC) was employed to study the influence of TiO_2 content on the non-isothermal crystallization behaviors of ESR-type slag. Continuous cooling transformation (CCT) diagrams of crystalline phases were plotted based on the DSC curves. The compositions and morphology of the crystalline phases were identified by X-ray diffraction (XRD) and a scanning electron microscope (SEM) equipped with energy dispersive spectroscopy (EDS). In addition, the effect of crystallization characteristics of the slag on the in-mold performance was discussed based on ESR pilot trials.

II. EXPERIMENTAL

A. *Sample Preparation*

The reagent-grade chemicals of $CaCO_3$ (≥ 99.0 mass pct), CaF_2 (≥ 99.0 mass pct), Al_2O_3 (≥ 99.99 mass pct), MgO (≥ 98.5 mass pct), and TiO_2 (≥ 98.0 mass pct) were used to produce slag samples. $CaCO_3$ powders were calcined at 1323 K (1050 °C) for 10 hours in a muffle furnace to produce CaO. The thoroughly mixed powders were premelted at 1773 K (1500 °C) in a platinum crucible for 5 minutes to homogenize their chemical composition. The liquid samples were quenched in iced water and crushed. The content of fluorine in the slag samples was determined by the ion-selective electrode method. The contents of aluminum, calcium, magnesium, and titanium were analyzed by inductively coupled plasma–atomic emission spectroscopy. The chemical compositions of the studied slag before and after premelting are shown in Table I.

B. *DSC Measurement*

DSC (Netzsch STA449F3; Netzsch Instrument Inc., Germany) measurements were taken under Ar gas atmosphere at 60 mL/min to evaluate the non-isothermal crystallization behaviors of the studied slag. Approximately 50 mg of sample powder was heated at the rate of 30 K/min from room temperature to 1773 K (1500 °C) in a platinum crucible with a diameter of 5 mm and a height of 5.5 mm and held for 1 minute to homogenize the chemical composition and eliminate bubbles; it was then cooled at various cooling rates (10, 15, 20, and 25 K/min) to 623 K (350 °C). The temperature history in the DSC measurement is shown in Figure 1. The thermal gravimetry recorded in the DSC thermal history showed that the weight loss of the slag samples was about 0.5 to 1.0 mass pct.

C. *SEM-EDS and XRD Analysis*

After DSC measurements, the slag samples were mounted with epoxy resin and then polished, followed with coating thin platinum film onto the polished sample to heighten the sample electric conductivity. The crystalline phases and crystal compositions of slag samples

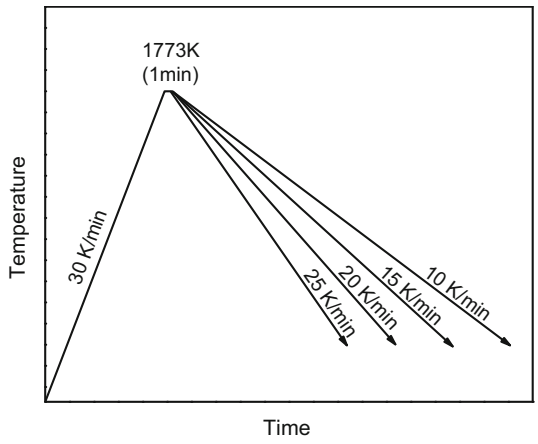

Figure 1—Thermal history in non-isothermal DSC measurements.

Table I. Chemical Compositions of the Studied Slag before and after Premelting (Mass Percent)

	Before Premelting					After Premelting				
Sample	CaF_2	CaO	Al_2O_3	MgO	TiO_2	CaF_2	CaO	Al_2O_3	MgO	TiO_2
R1	30	32	32	2	4	26.3	35.6	31.4	2.5	4.2
R2	30	30	30	2	8	25.0	34.7	29.5	2.5	8.4
R3	30	28	28	2	12	26.2	31.3	27.5	2.4	12.6
R4	30	26	26	2	16	25.8	29.6	25.3	2.5	16.8

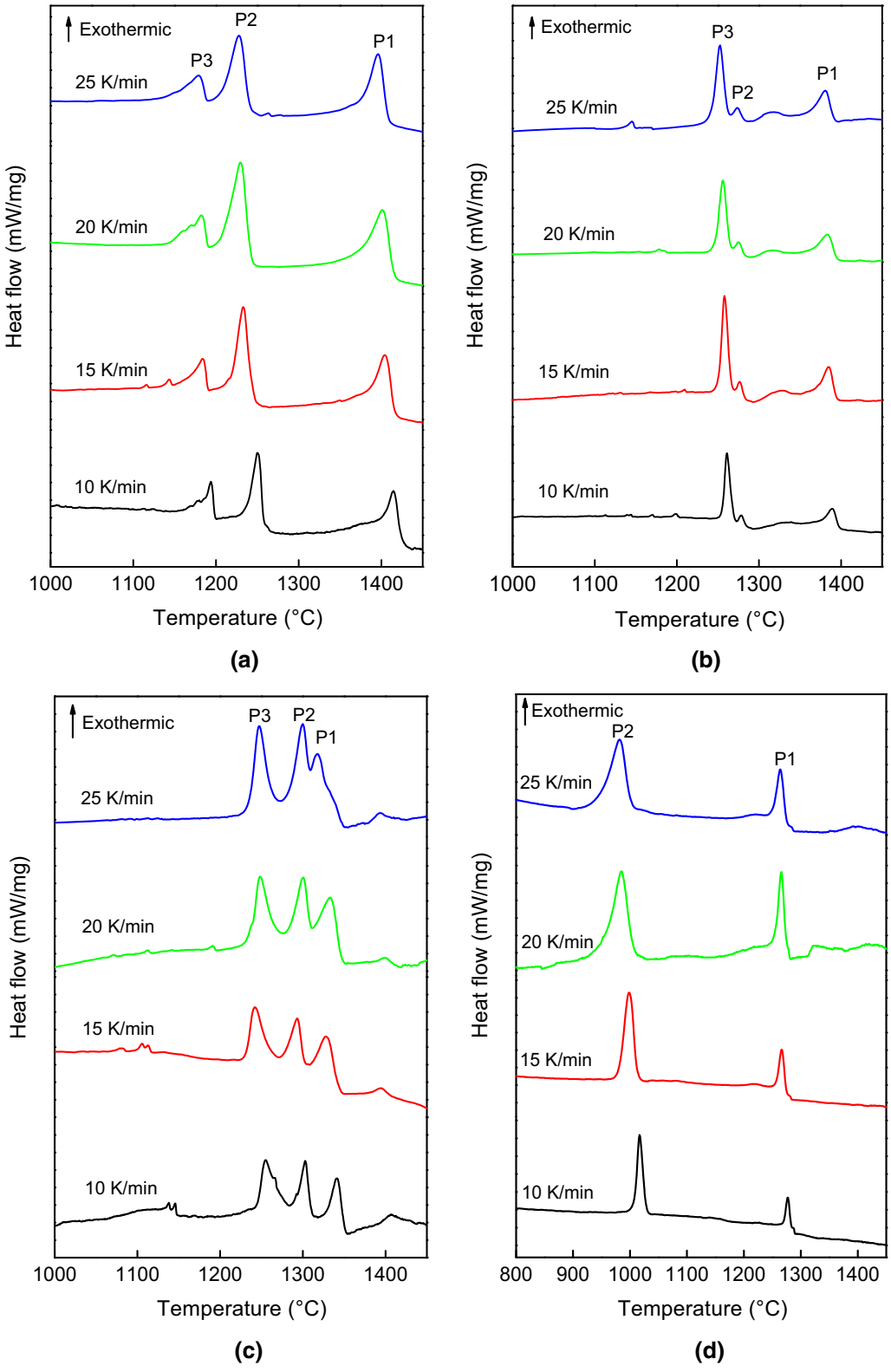

Figure 2—DSC curves of non-isothermal crystallization of slag melts at various cooling rates: (*a*) slag R1, (*b*) slag R2, (*c*) slag R3, and (*d*) slag R4.

after DSC measurements were identified by SEM (FEI Quanta-250; FEI Corporation, Hillsboro, OR) equipped with EDS (XFlash 5030; Bruker, Germany).

Because of the small amount of the slag after DSC measurements, it is hard to identify the crystalline phases in the slag by XRD, a sequence of continuous cooling experiments was executed based on the corresponding temperature of each exothermic peak of DSC curves to identify the crystalline phase of the slag samples. Approximately 1 g of sample powder was melted in a platinum crucible at 1773 K (1500 °C) for 1 minute and subsequently cooled in a muffle furnace to the corresponding temperature; it was then held for 30 minutes. Then, the slag samples were quenched by iced water and ground into powders to determine the crystalline phases by XRD with Cu K_a radiation.

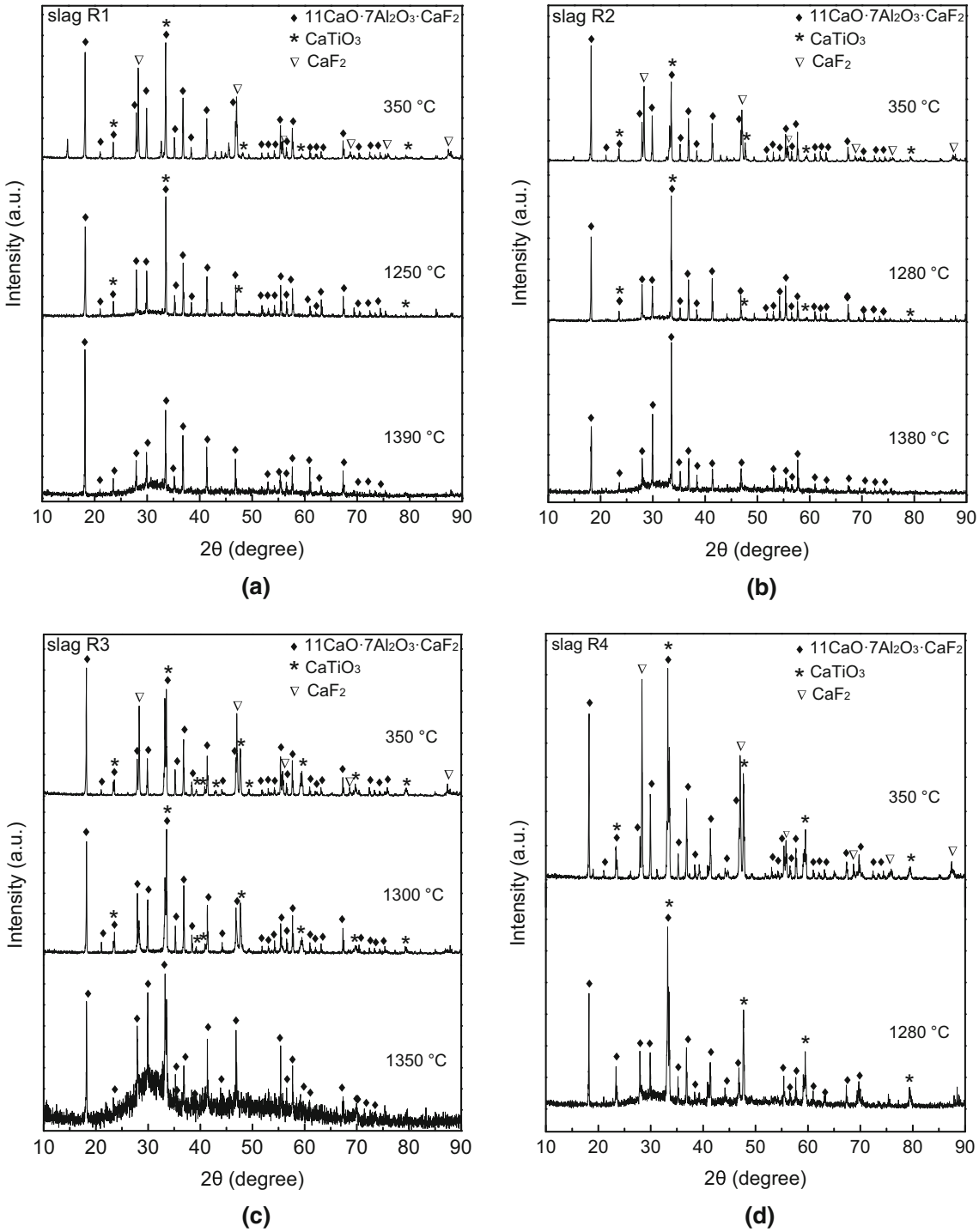

Figure 3—XRD patterns of the slag quenched at desired temperatures: (*a*) slag R1, (*b*) slag R2, (*c*) slag R3, and (*d*) slag R4.

III. RESULTS AND DISCUSSION

A. *Non-isothermal DSC Measurement and XRD Identification*

Figure 2 presents the effect of TiO_2 content on the DSC cooling curves of slag samples at various cooling rates of 10, 15, 20, and 25 K/min, respectively. The exothermic peak on the DSC curve is an indication of crystalline phase precipitation. As shown in Figure 2, three exothermic peaks were found on the DSC cooling curves for slag R1, R2, and R3, and only two distinct exothermic peaks for slag R4 at each cooling rate, indicating the presence of three crystallization events for slag R1, R2, and R3 and two crystallization events for slag R4. The peaks are named P1, P2, and P3, respectively.

The XRD patterns of the slag samples quenched at the different temperatures are presented in Figure 3. The cooling rate of heat treatment is 5 K/min, which is less than that in the DSC experiments because of the limited abilities of the furnace. However, the different cooling rate here has no influence on the precipitation sequence of the crystalline phase. Three crystalline phases were identified at 623 K (350 °C) in each slag by XRD, *i.e.*, $11CaO{\cdot}7Al_2O_3{\cdot}CaF_2$, $CaTiO_3$, and CaF_2. It is shown from Figures 3(a) through (c) that the sequence of crystal precipitation during cooling of the slag R1, R2, and R3 is $11CaO{\cdot}7Al_2O_3{\cdot}CaF_2$ (designated as p1) to

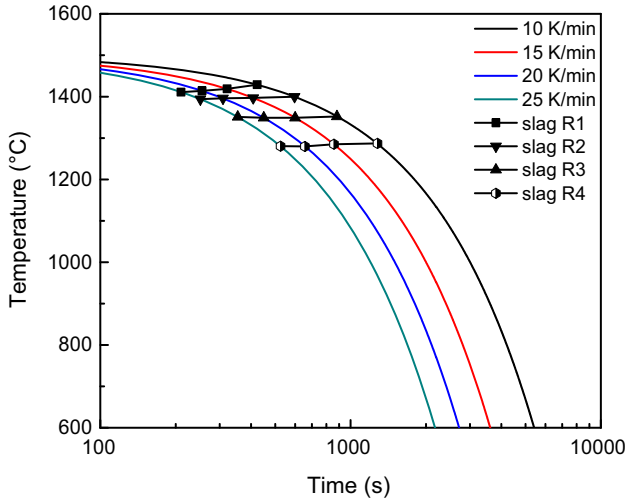

Figure 5—CCT diagram for the first crystalline phases precipitated in the slag.

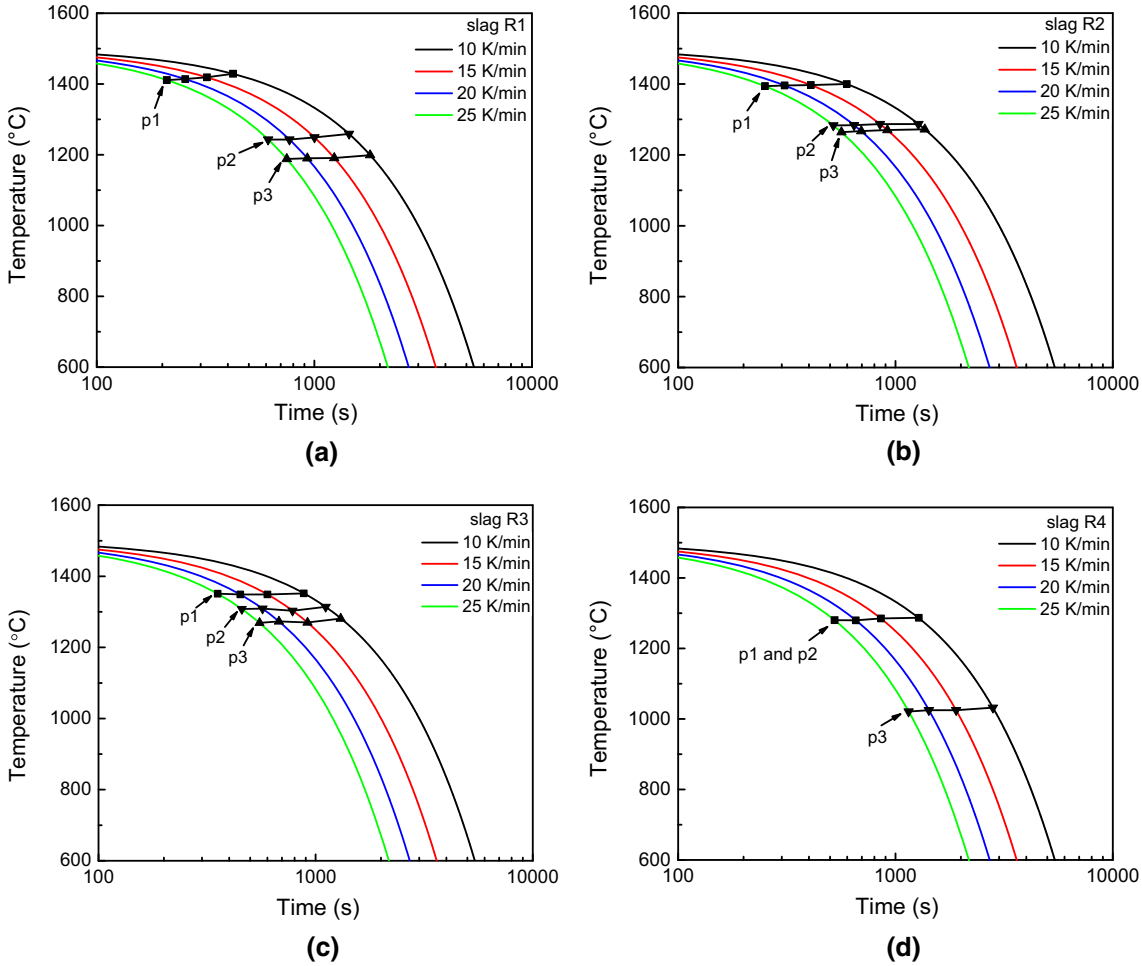

Figure 4—CCT diagrams of slag samples with different TiO_2 contents: (*a*) slag R1, (*b*) slag R2, (*c*) slag R3, and (*d*) slag R4.

$CaTiO_3$ (designated as p2), followed by CaF_2 (designated as p3). The exothermic peaks P1, P2, and P3 represent the precipitation of $11CaO{\cdot}7Al_2O_3{\cdot}CaF_2$, $CaTiO_3$, and CaF_2, respectively. Figure 3(d) shows that the crystalline phases in slag R4 quenched at 623 K (350 °C) are identified as $11CaO{\cdot}7Al_2O_3{\cdot}CaF_2$, $CaTiO_3$, and CaF_2. However, only two exothermic peaks were found on DSC curves with various cooling rates in Figure 2(d). The exothermic peak P1 represents the precipitation of $11CaO{\cdot}7Al_2O_3{\cdot}CaF_2$ and $CaTiO_3$ and the exothermic peak P2 represents the precipitation of CaF_2 in Figure 2(d). This may be due to the fact that the precipitation of $11CaO{\cdot}7Al_2O_3{\cdot}CaF_2$ and $CaTiO_3$ took place simultaneously in slag R4 during continuous cooling. A similar finding was reported by Seo *et al.*[19] Therefore, the sequence of crystal precipitation during cooling of slag R4 is that $11CaO{\cdot}7Al_2O_3{\cdot}CaF_2$ and $CaTiO_3$ precipitate at the same time, followed by CaF_2. The XRD results are consistent with the SEM-EDS results, which will be given in the Section III–C.

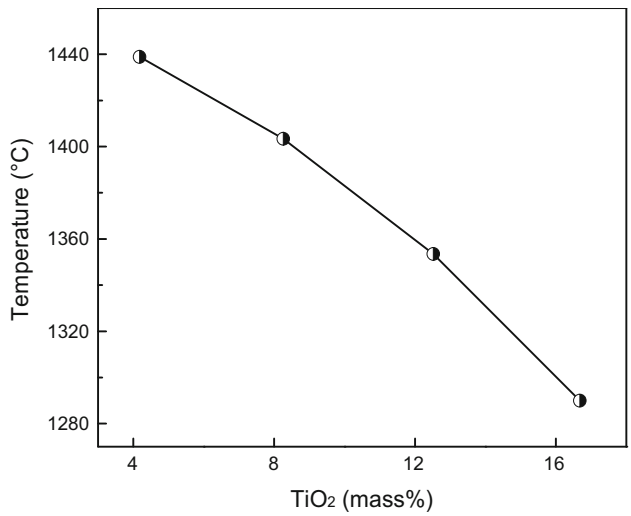

Figure 6—Change of liquidus temperature of the slag with different TiO_2 contents.

B. *Crystallization Temperature and Liquidus Temperature of the Slag*

The onset temperature of the exothermic peak during continuous cooling can be defined as the crystallization temperature of crystalline phase, at which the crystalline phase starts to precipitate during the non-isothermal crystallization process. The CCT diagrams of the crystalline phases in the slag were constructed to clarify the crystallization tendency of the slag based on the time-temperature profiles and the crystallization temperature recorded in DSC curves with various cooling rates, as shown in Figure 4. It is clear that the crystallization temperatures of the crystalline phases in the slag increase with the decreasing cooling rate in DSC measurements. This is expected to be attributed to the fact that a stronger driving force is required to promote the nucleation in the slag melts with increasing the cooling rate of the slag.[20,21] Accordingly, the crystallization temperature decreases with the increasing cooling rate to provide larger undercooling for the nucleation. The lower cooling rate is beneficial to the precipitation of the crystalline phase, and the crystallization temperature correspondingly decreases at a higher cooling rate.

Figure 5 presents the CCT diagram for the precipitation of the first crystalline phases in the slag melts. The precipitation temperature of the first crystalline phase during the continuous cooling process correspondingly is defined as the crystallization temperature of the slag. It can be seen from Figure 5 that the precipitation temperatures of the first crystalline phases are found to decrease with increasing TiO_2 content in the slag. This

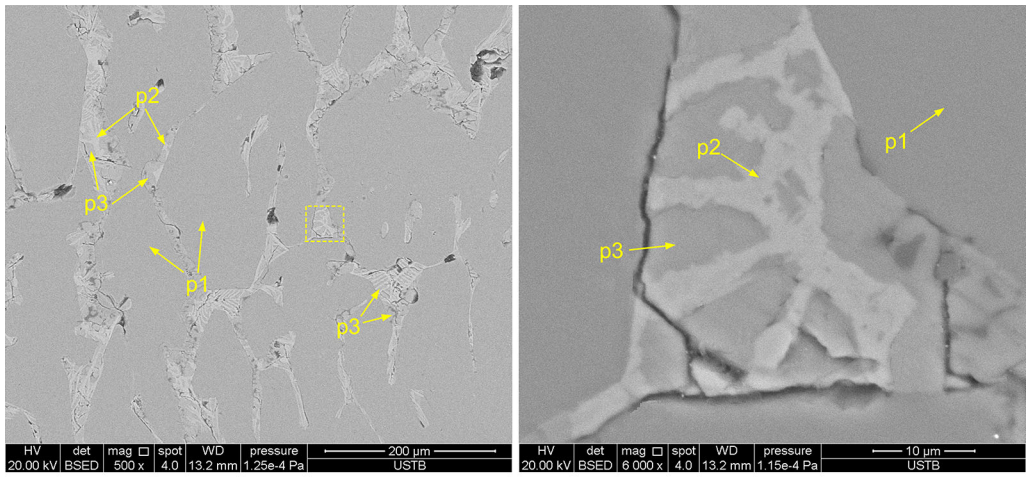

(a) (b)

Figure 7—(*a*) and (*b*) SEM results of slag R1 after DSC measurement at the cooling rate of 10 K/min. (b) is an enlarged image of the enclosed area of (a).

result also agrees with the findings that the crystallization temperatures of other metallurgical slags decrease with increasing TiO_2 content.[22–24]

Liquidus temperature is the temperature at which solid slag is fully transformed into liquid, and it can be obtained by extrapolating the crystallization temperatures of slag melts at the various cooling rates of 10, 15, 20, and 25 K/min to the value with the cooling rate of 0 K/min. Figure 6 presents the liquidus temperature of molten slag with different TiO_2 contents. It could be found that the liquidus temperature of slag decreased from 1712 K to 1563 K (1439 °C to 1290 °C) with increasing TiO_2 content from 4.2 to 16.8 mass pct in the slag, suggesting that the crystallization tendency of the studied ESR-type TiO_2-bearing slag decreases with the addition of TiO_2. The liquidus temperatures of the slag calculated with FactSage 6.4 using CON2 database (ThermFact/CRCT, Montréal, Canada) are 1678 K (1405 °C), 1652 K (1379 °C), 1640 K (1367 °C), and 1696 K (1423 °C) for slag R1, R2, R3, and R4, respectively. There are some deviations between the calculated and the experimental liquidus temperatures, which may be because the FactSage calculation of the crystalline phase evolution is based on infinite equilibrium and the kinetic limitation of the crystalline phase formation is not taken into account in the thermodynamic calculation.

The crystallization temperature is one of most important factors determining the surface quality of the as-cast ESR ingot. With the proper decrease in the crystallization temperature of the slag, it is beneficial to form a thinner slag skin and stable heat flux across the slag skin, which provides a sound condition for the good surface quality of the as-cast ingot.[5,25] Therefore, the

Table II. Compositions of Crystals Determined by EDS in the Slag Samples after DSC Measurement at the Cooling Rate of 10 K/min, Corresponding to the SEM Results Shown in Figs. 7 through 13

		Element (Atomic Percent)					
Figures	Phase	Ca	Al	Ti	F	O	Mg
7(b)	p1	24.5	26.8	—	3.7	46.1	—
	p2	23.9	3.0	20.6	—	52.5	—
	p3	35.3	1.1	—	63.0	—	—
9(b)	p1	23.6	24.7	—	3.7	48.0	—
	p2	23.6	2.8	20.6	—	53.0	—
	p3	37.0	—	—	63.0	—	—
	glass	26.3	4.2	—	27.3	31.3	10.5
11(b)	p1	24.2	26.8	—	4.2	46.7	—
	p2	24.6	2.8	21.6	—	50.4	—
	p3	37.0	—	—	63.0	—	—
	glass	5.8	23.4	1.2	4.4	51.0	14.4
13(b)	p1	27.5	27.2	—	4.3	41.0	—
	p2	27.4	2.3	25.4	—	44.9	—
	p3	39.3	—	—	60.7	—	—
	glass	16.1	18.8	0.7	19.2	42.2	3.0

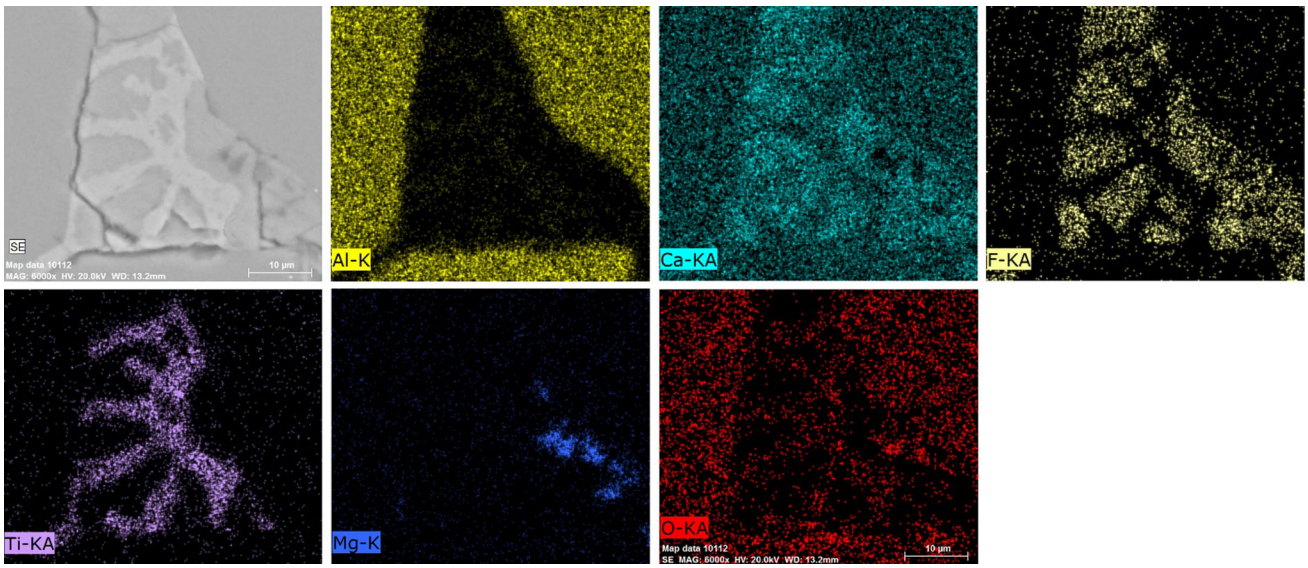

Figure 8—Element mappings of crystals in slag R1 after DSC measurement at the cooling rate of 10 K/min.

surface quality of the as-cast ESR ingot is gradually improved in the case where the TiO_2 content, which could originate from the accumulation of TiO_2 in the slag pool during ESR of Ti-containing steel and alloy, is in a proper range (4.2 to 16.8 mass pct in the present slag). The effect of crystallization characteristics on the in-mold performance of the studied slag was verified by the ESR pilot trials operating in a static mode, and the results will be shown in Section III–D.

C. *SEM-EDS Observation of the Crystals in the Slag*

To reveal the influence of molten slag crystallization on heat transfer, the morphologies and compositions of crystalline phases in slag samples after DSC experiments were identified by SEM-EDS. The crystalline phases can be determined by combining the XRD with the SEM-EDS results. Figures 7 through 14 show the SEM-EDS results of the solidified slag after DSC measurements. Considering the fact shown in Figure 2 that the cooling rate has no influence on the types of crystalline phases in each slag after DSC measurements, only the compositions of crystalline phases in the slag at the cooling rate of 10 K/min, except slag R4 with all four cooling rates, were determined by SEM-EDS. The EDS results are listed in Table II. It can be seen from the SEM results that three crystalline phases were found in the four slag samples, which is consistent with the XRD results. According to the EDS results shown in Table II and the XRD patterns presented in Figure 3, the three crystalline phases found in the SEM micrographs of the solidified slag are determined to be $11CaO{\cdot}7Al_2O_3{\cdot}CaF_2$, $CaTiO_3$, and CaF_2.

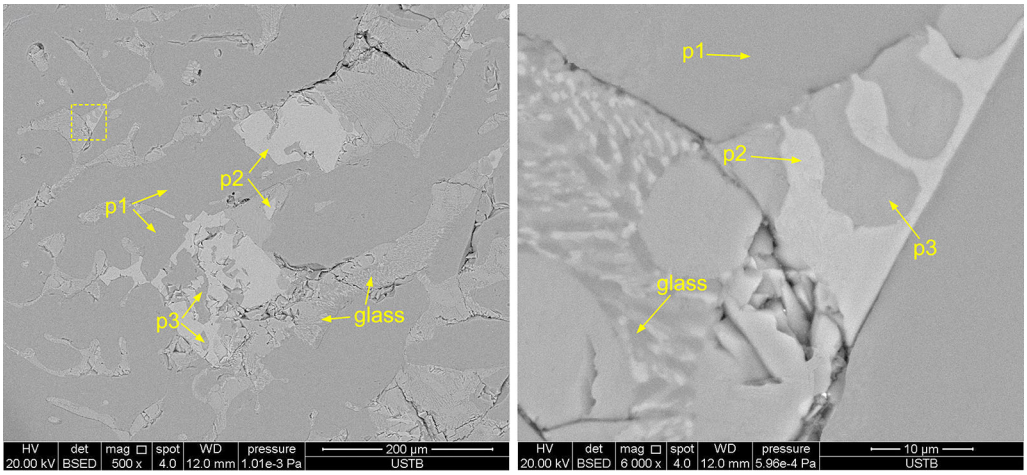

Figure 9—(*a*) and (*b*) SEM results of slag R2 after DSC measurement at the cooling rate of 10 K/min. (b) is an enlarged image of the enclosed area of (a).

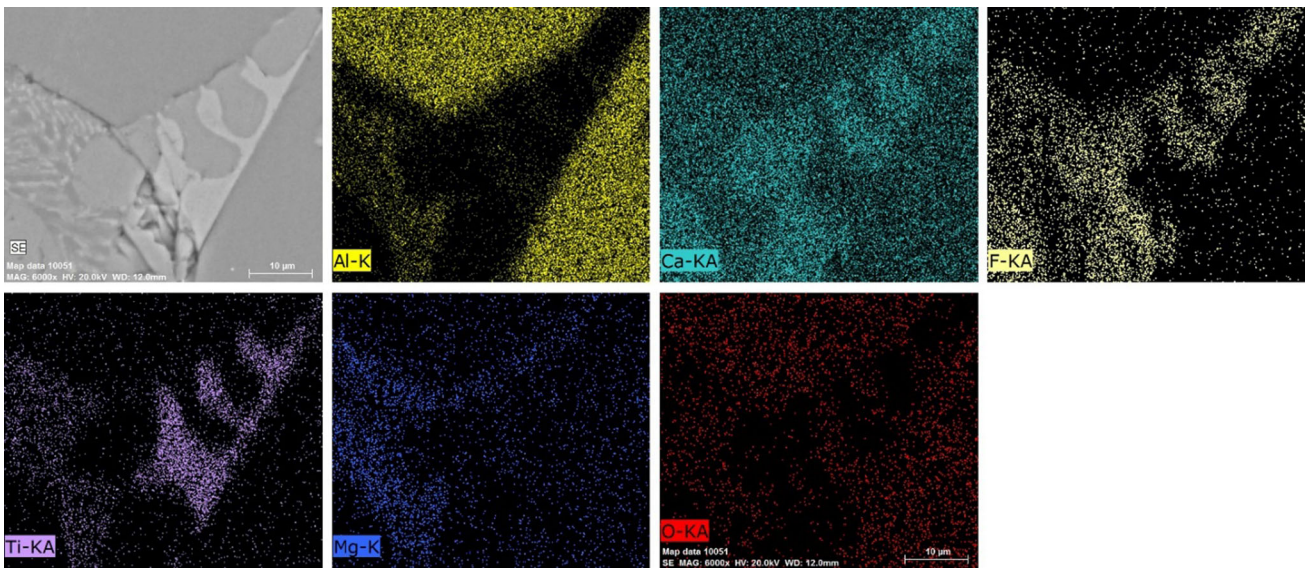

Figure 10—Element mappings of crystals in slag R2 after DSC measurement at the cooling rate of 10 K/min.

Figures 7 and 8 show the SEM-EDS results of slag R1 after DSC measurement at the cooling rate of 10 K/min. A large amount of faceted $11CaO{\cdot}7Al_2O_3{\cdot}CaF_2$ crystals precipitated first, and near-spherical CaF_2 crystals precipitated in the crevices of bonelike $CaTiO_3$. It was found that a small amount of Mg enriched in the solidified slag, indicating that a small amount of MgO precipitated from slag R1. The precipitation of MgO can be ignored because both the content of MgO in the original slag and the precipitated amount of MgO in slag R1 shown in Figure 7(a) are low.

Figures 9 and 10 show the SEM-EDS results of slag R2 after DSC measurement at the cooling rate of 10 K/min. As shown in Figure 9(a), the $11CaO{\cdot}7Al_2O_3{\cdot}CaF_2$ crystals with faceted morphology are the dominant crystalline phase and occupy the largest crystalline fraction. Spherical CaF_2 precipitated in the crevices of $CaTiO_3$. It can be seen from Figures 7(a) and 9(a) that the morphology of $CaTiO_3$ crystals changes from bonelike to bonelike and block.

Figures 11 and 12 show the SEM-EDS results of slag R3 after DSC measurement at the cooling rate of 10 K/min. The faceted $11CaO{\cdot}7Al_2O_3{\cdot}CaF_2$ crystals are still the dominant crystalline phase, as shown in Figure 11(a), but the crystalline fraction of $11CaO{\cdot}7Al_2O_3{\cdot}CaF_2$ crystals is obviously smaller than that in Figures 7(a) and 9(a). The precipitated amount of $CaTiO_3$ increases significantly, and the $CaTiO_3$ crystals are uniformly distributed in the solidified slag. The morphology of CaF_2 crystals is spherical.

Figure 13 shows the SEM results of slag R4 after DSC measurements at different cooling rates. Three crystalline phases are found in Figure 13(b), which agree with the XRD results. The element mapping results shown in Figure 14 suggest that the crystalline phases in solidified slag R4 are $11CaO{\cdot}7Al_2O_3{\cdot}CaF_2$, $CaTiO_3$, and CaF_2. It is clear from Figure 13 that the dominant crystalline phase is blocky $CaTiO_3$ crystals, which exhibit in various sizes and take up most of the crystalline fraction in slag R4. As shown in Figure 13(b), the morphology of CaF_2 crystals is spherical.

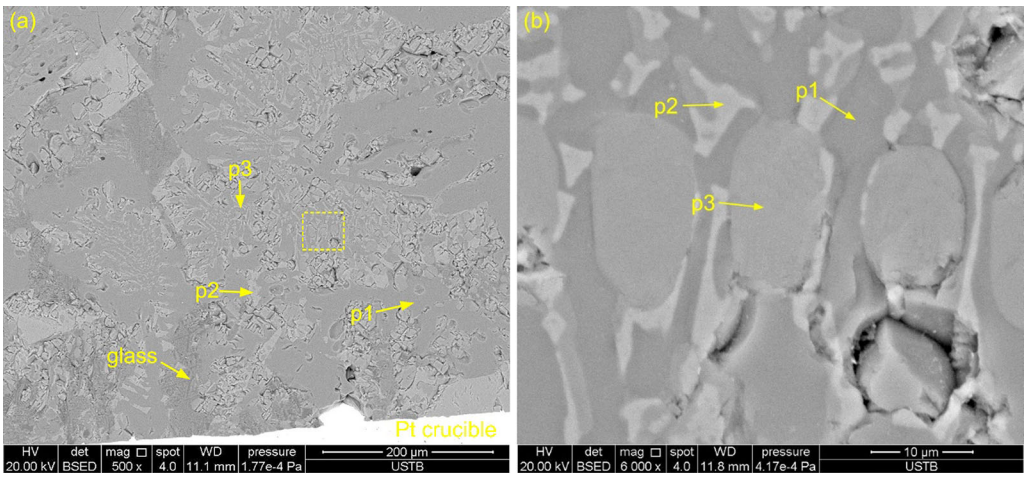

Figure 11—(*a*) and (*b*) SEM results of slag R3 after DSC measurement at the cooling rate of 10 K/min. (b) is an enlarged image of the enclosed area of (a).

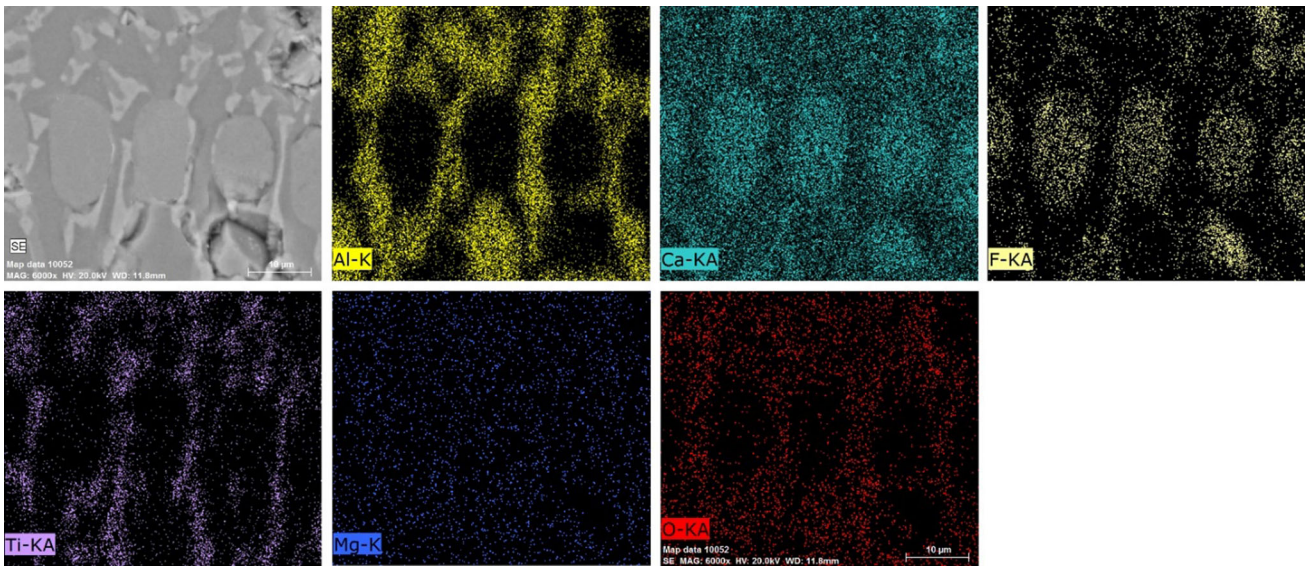

Figure 12—Element mappings of crystals in slag R3 after DSC measurement at the cooling rate of 10 K/min.

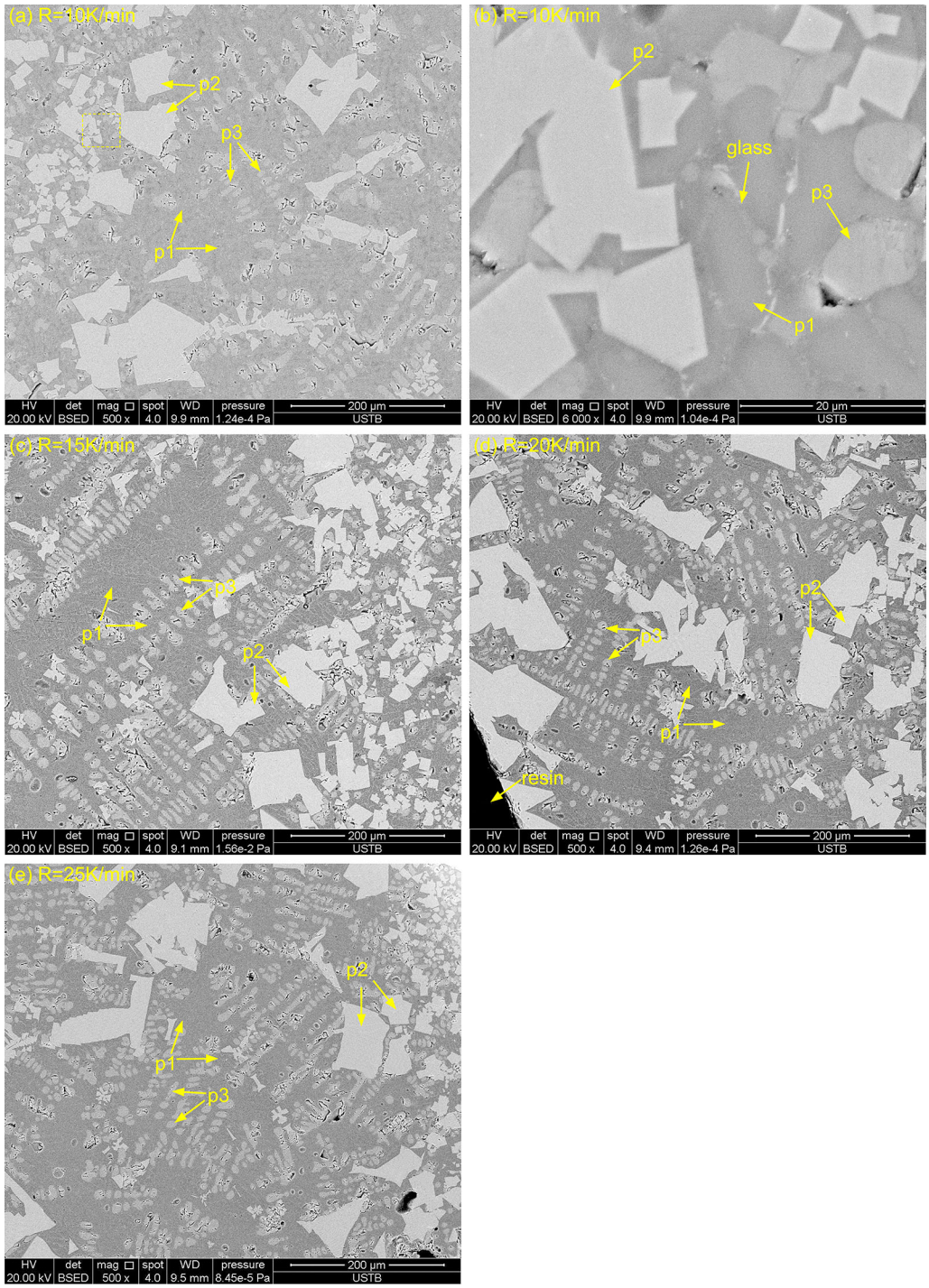

Figure 13—SEM results of slag R4 after DSC measurement at various cooling rates: (*a*) 10 K/min, (*b*) 10 K/min, (*c*) 15 K/min, (*d*) 20 K/min, and (*e*) 25 K/min. (b) is an enlarged image of the enclosed area of (a).

$11CaO{\cdot}7Al_2O_3{\cdot}CaF_2$ crystals have elliptically faceted morphology, and the size of these crystals is obviously smaller than that in the other three slag melts at the continuous cooling rate of 10 K/min.

Therefore, there is no change in the types of crystalline phase in the studied ESR-type TiO_2-bearing slag with different TiO_2 contents ranging from 4.2 to 16.8 mass pct during continuous cooling, *i.e.*, $11CaO{\cdot}7Al_2O_3{\cdot}CaF_2$, $CaTiO_3$, and CaF_2. With the addition of TiO_2 in the slag, the dominant crystalline phase changes from $11CaO{\cdot}7Al_2O_3{\cdot}CaF_2$ to $CaTiO_3$. The morphology of $11CaO{\cdot}7Al_2O_3{\cdot}CaF_2$ is faceted or elliptically faceted for the four slag. The morphology of $CaTiO_3$ changes from bonelike to blocky. The morphology of CaF_2 is spherical in all cases, irrespective of the TiO_2 contents in the slag.

According to the XRD results, $11CaO{\cdot}7Al_2O_3{\cdot}CaF_2$ is the first crystalline phase precipitated in each slag melt, although $11CaO{\cdot}7Al_2O_3{\cdot}CaF_2$ and $CaTiO_3$ precipitate at the same time in solidified slag R4. The SEM results suggest that the morphology of $11CaO{\cdot}7Al_2O_3{\cdot}CaF_2$ is faceted. The morphology of the crystalline phase is mainly dependent on the growth process, which consists of the element diffusion from the liquid to the interface and the interfacial chemical reactions.[26] The crystalline phase with dendritic morphology and that with faceted morphology indicate that the crystallization behavior is controlled by element diffusion and interfacial chemical reaction, respectively.[26,27] Therefore, the crystallization of $11CaO{\cdot}7Al_2O_3{\cdot}CaF_2$ is controlled by interfacial chemical reaction. This result is similar to the finding for the $CaO\text{-}Al_2O_3$–based TiO_2-bearing mold fluxes reported by Li *et al.*[14] The activities of components in the slag at 1500 °C were calculated by FactSage 6.4 (CON2 database), as shown in Figure 15. CaO, Al_2O_3, and CaF_2 are the components for $11CaO{\cdot}7Al_2O_3{\cdot}CaF_2$ formation. With the addition of TiO_2 from 4.2 to 16.8 mass pct in the slag, the activity of CaO decreases obviously while the activities of Al_2O_3 and CaF_2 increase in the slag melts. It can be deduced that increasing the TiO_2 content diminishes the available CaO content as the main component of $11CaO{\cdot}7Al_2O_3{\cdot}CaF_2$ formation, which results in deferring the formation of $11CaO{\cdot}7Al_2O_3{\cdot}CaF_2$.

D. *In-Mold Performance of the ESR-Type TiO_2-Bearing Slag*

The mechanism of slag skin formation and its influence on the ESR ingot surface have been revealed in detail elsewhere.[28–30] For ESR operating in a static mode, the liquid metal pool moves upward during the ESR process. The temperature at the front of the solidification shell should be higher than the crystallization temperature of the slag. The slag skin, which has solidified above the liquid metal pool near the mold, is partially remelted adequately as the rising of the liquid metal pool. In this case, the heat flux across the slag skin is relatively stable. Therefore, the slag with appropriate crystallization temperature forms a thin and smooth slag skin, which is conducive to surface quality of the as-cast ingot.

However, the slag skin could not be remelted when using the slag with higher crystallization temperature, causing the formation of thicker slag skin and a concave solidification steel shell. The heat flux across the slag skin decreases with the increase of the slag skin thickness, resulting in the gradual increase in the temperature at the front of the solidification shell. Consequently, the slag skin is remelted again, which gives rise to the formation of thinner slag skin and a convex solidification steel shell. As a result of the

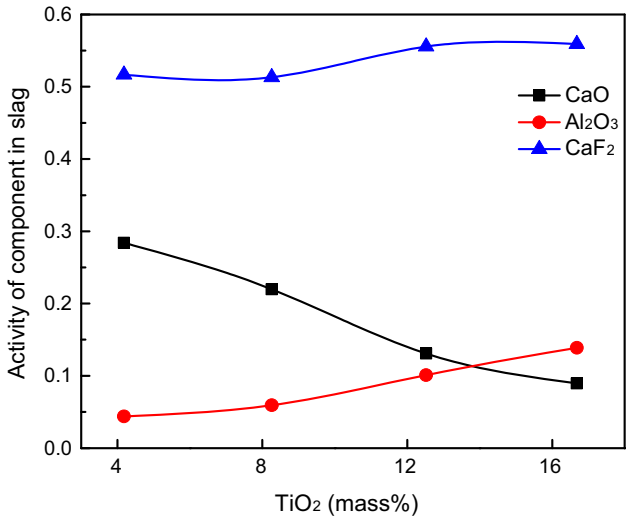

Figure 15—Activity of components in the slag against TiO_2 content at 1500 °C.

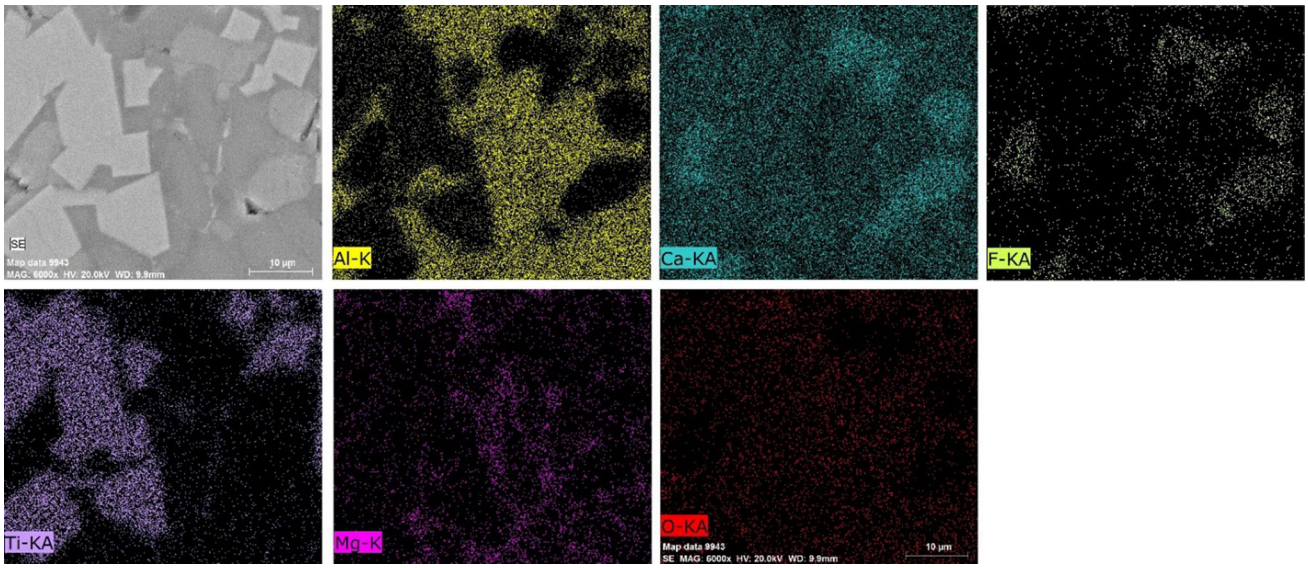

Figure 14—Element mappings of crystals in slag R3 after DSC measurement at the cooling rate of 10 K/min.

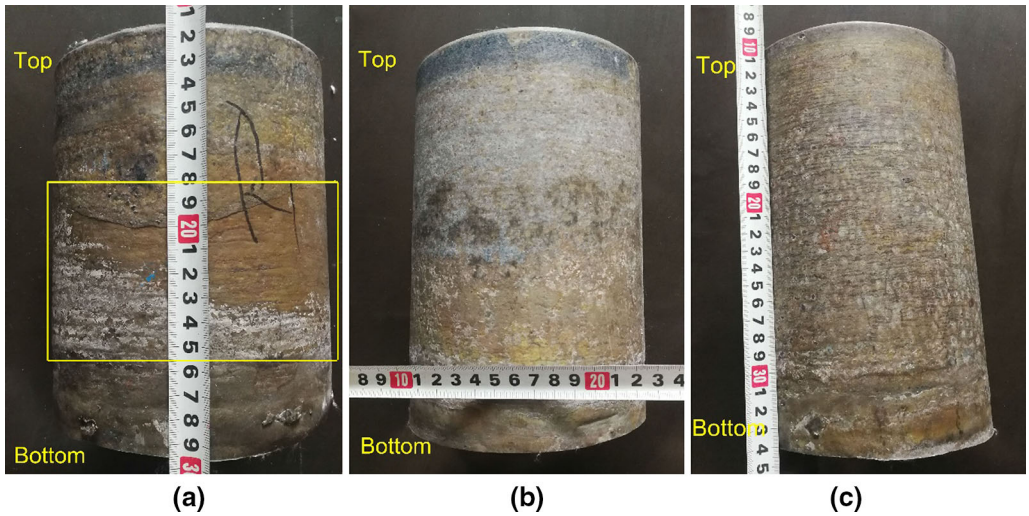

Figure 16—Photographs of ESR ingot surfaces after ESR pilot trials using the studied slag: (*a*) slag R1, (*b*) slag R2, and (*c*) slag R3.

repetition of the preceding process, there will be defects at the surface of the as-cast ESR ingots, such as dent marks and ripple defects on the ingot surface.

The application of the studied ESR-type TiO_2-bearing slag has been performed in the ESR pilot trials operating in a static mode. According to the designed chemical composition, the industrial fluorite, lime, alumina, magnesia, and titanium dioxide were mixed and then premelted. The consumable electrodes had a diameter of 80 mm and a height of 1100 mm.

Figure 16 presents the photographs of the surface appearance of the ESR ingots (130 mm in diameter and about 200 mm in length) produced by using slag with 5.66, 9.51, and 13.77 mass pct TiO_2. It can be seen from Figure 16(a) that many ripples are observed on the surface of the ESR ingots, especially in the marked region. The frequent change of the heat flux across the slag skin induced by the higher crystallization temperature of slag R1 results in the appearance of ripples at the surface of the ESR ingot. With the increase in TiO_2 content in the ESR slag, the surface quality of the ESR ingot has been improved when using slag R2 and R3, as shown in Figures 16(b) and (c). The effect of TiO_2 content on the crystallization behavior of the studied ESR-type TiO_2-bearing slag can be confirmed by the ESR pilot trials.

IV. CONCLUSIONS

The non-isothermal crystallization characteristics of the ESR-type TiO_2-bearing slag were studied by DSC, XRD, and SEM-EDS. The effect of crystallization characteristics of the slag on the in-mold performance was verified by ESR pilot trials operating in a static mode. The conclusions are summarized as follows.

1. Increasing TiO_2 content decreased the crystallization temperature and liquidus temperature of the slag and suppressed the crystallization tendency of the slag. The liquidus temperature of slag decreased from 1712 K to 1563 K (1439 °C to 1290 °C) with increasing TiO_2 content from 4.2 to 16.8 mass pct in the slag.
2. There is no change in the types of the crystalline phases in the slag with different TiO_2 contents during cooling, *i.e.*, $11CaO{\cdot}7Al_2O_3{\cdot}CaF_2$, $CaTiO_3$, and CaF_2. The sequence of crystal precipitation during cooling was $11CaO{\cdot}7Al_2O_3{\cdot}CaF_2$ to $CaTiO_3$, followed by CaF_2 with increasing TiO_2 content from 4.2 to 12.6 mass pct. With adding 16.8 mass pct TiO_2, the precipitation of $11CaO{\cdot}7Al_2O_3{\cdot}CaF_2$ and $CaTiO_3$ took place simultaneously, followed by CaF_2.
3. With the addition of TiO_2 in the slag, the dominant crystalline phase changes from $11CaO{\cdot}7Al_2O_3{\cdot}CaF_2$ crystals to $CaTiO_3$ crystals. The morphology of $11CaO{\cdot}7Al_2O_3{\cdot}CaF_2$ and $CaTiO_3$ changes from faceted and bonelike to elliptically faceted and blocky, respectively. The morphology of CaF_2 is spherical in all cases.
4. The decrease in the crystallization tendency of the slag with increasing TiO_2 contents is attributed to the decrease in the activity of CaO in the slag.
5. Increasing TiO_2 content in the slag is favorable for providing thin slag skin and stable heat flux across the slag skin, which improved the surface quality of the as-cast ESR ingot.

ACKNOWLEDGMENTS

The authors are sincerely grateful to Professor Jung-wook Cho, Pohang University of Science and Technology, for his help in using the FactSage software. The financial support by the National Natural Science Foundation of China (Grant Nos. 51774225, 51874030, and 51874026) and the Fundamental Research Funds for the Central Universities (Grant No. FRF-TP-18-004A3) is greatly acknowledged.

REFERENCES

1. M. Eissa and A. Ei-Mohammad: *Steel. Res.*, 1998, vol. 69, pp. 413–17.
2. C.B. Shi, H. Wang, and J. Li: *Metall. Mater. Trans. B*, 2018, vol. 49B, pp. 1675–89.
3. A. Ahmed and A. Fathy: *Ironmak. Steelmak.*, 2008, vol. 35, pp. 458–64.
4. C.B. Shi, W.T. Yu, H. Wang, J. Li, and M. Jiang: *Metall. Mater. Trans. B*, 2017, vol. 48B, pp. 146–61.
5. C.B. Shi, J. Li, J.W. Cho, F. Jiang, and I.H. Jung: *Metall. Mater. Trans. B*, 2015, vol. 46B, pp. 2110–20.
6. Z.X. Xue, Y.X. Zheng, F. Jiang, Y.Q. Du, B.S. Guo, P. Lin, and C.B. Shi: *Special Steel*, 2016, vol. 37, pp. 37–40 (in Chinese).
7. X.C. Lu: *Foundry*, 2002, vol. 51, pp. 378–80 (in Chinese).
8. H.Y. Zhao: *Special Steel*, 2006, vol. 27, pp. 61–62 (in Chinese).
9. G. Pateisky, H. Biele, and H.J. Fleischer: *J. Vac. Sci. Technol.*, 1972, vol. 9, pp. 1318–21.
10. C.B. Shi, M.D. Seo, J.W. Cho, and S.H. Kim: *Metall. Mater. Trans. B*, 2014, vol. 45B, pp. 1081–97.
11. X.M. Li, S.J. Wang, J.X. Zhao, Y.R. Cui, and Y.M. Chen: *Adv. Mater. Res.*, 2011, vols. 239–242, pp. 1960–63.
12. X. Li, X. Geng, Z.H. Jiang, H.B. Li, F.H. Xu, and L.X. Wang: *Iron Steel*, 2015, vol. 50, pp. 41–46 (in Chinese).
13. C.B. Shi, J.W. Cho, D.L. Zheng, and J. Li: *Int. J. Miner. Metall. Mater.*, 2016, vol. 23, pp. 627–36.
14. J.L. Li, Q.F. Shu, X.M. Hou, and K.C. Chou: *ISIJ Int.*, 2015, vol. 55, pp. 830–36.
15. D.D.R. Silva, A.C.F. Vilela, N.C. Heck, H.P. Heller, and O. Volkova: *Steel. Res. Int.*, 2018, https://doi.org/10.1002/srin.201700246.
16. Z.Q. Hao, W.Q. Chen, C. Lippold, and H.X. Mao: *Chin. J. Process Eng.*, 2009, vol. 9, pp. 514–18 (in Chinese).
17. J.A. Bothma and P.C. Pistorius: *Ironmak. Steelmak.*, 2007, vol. 34, pp. 513–20.
18. M.L. Hu, R.R. Wei, F.F Yin, L. Liu, and Q.Y. Deng: *JOM*, 2016, vol. 68, pp. 2502–10.
19. M.D. Seo, J.W. Cho, and S.H. Kim: *Metall. Mater. Trans. B*, 2014, vol. 45B, pp. 1874–86.
20. M.D. Seo, C.B. Shi, J.Y. Baek, J.W. Cho, and S.H. Kim: *Metall. Mater. Trans. B*, 2015, vol. 46B, pp. 2374–83.
21. L.J. Zhou, W.L. Wang, F.J. Ma, J. Li, J. Wei, H. Matsuura, and F. Tsukihashi: *Metall. Mater. Trans. B*, 2012, vol. 43B, pp. 354–62.
22. L.S. Li, X.R. Wu, L. Yu, and Y.C. Dong: *Ironmak. Steelmak.*, 2008, vol. 35, pp. 367–70.
23. Z.J. Wang, Y.Q. Sun, S. Sridrar, M. Zhang, and Z.T. Zhang: *Metall. Mater. Trans. B*, 2017, vol. 48B, pp. 527–37.
24. J. Li, Z.T. Zhang, L.L. Liu, W.L. Wang, and X.D. Wang: *ISIJ Int.*, 2013, vol. 53, pp. 1696–1703.
25. Z.H. Jiang and X. Geng: *Adv. Mater. Res.*, 2010, vols. 146–147, pp. 670–73.
26. J. Guo, M.D. Seo, C.B. Shi, J.W. Cho, and S.H. Kim: *Metall. Mater. Trans. B*, 2016, vol. 47B, pp. 2211–21.
27. M. Asanishi, T. Takaki, and Y. Tomita: *AES-ATEMA Int. Conf. Ser.*, 2007, pp. 195–203.
28. L. Zhao, D.G. Jin, J.J. Gao, Z.H. Zhou, and X.H. Liu: *Heavy Casting Forging*, 1997, vol. 3, pp. 22–27 (in Chinese).
29. A. Mitchell and M. Etienne: *Trans. TMS-AIME*, 1968, vol. 242, pp. 1462–64.
30. M. Bell and A. Mitchell: *J. Iron Steel Inst.*, 1971, vol. 209, pp. 658–70.